Automated lithological mapping using airborne hyperspectral thermal infrared data: A case study from Anchorage Island, Antarctica

Martin Black[a,b], Teal R. Riley[a], Graham Ferrier[b], Andrew H. Fleming[a], Peter T. Fretwell[a]

[a] *British Antarctic Survey, High Cross, Madingley Road, Cambridge, CB3 0ET, UK.*
[b] *University of Hull, Department of Geography, Environment and Earth Sciences, Cottingham Road, Hull, HU6 7RX, UK.*

Abstract

The thermal infrared portion of the electromagnetic spectrum has considerable potential for mineral and lithological mapping of the most abundant rock-forming silicates that do not display diagnostic features at visible and shortwave infrared wavelengths. Lithological mapping using visible and shortwave infrared hyperspectral data is well developed and established processing chains are available, however there is a paucity of such methodologies for hyperspectral thermal infrared data. Here we present a new fully automated processing chain for deriving lithological maps from hyperspectral thermal infrared data and test its applicability using the first ever airborne hyperspectral thermal data collected in the Antarctic. A combined airborne hyperspectral survey, targeted geological field mapping campaign and detailed mineralogical and geochemical datasets are applied to small test site in West Antarctica where the geological relationships are representative of continental margin arcs. The challenging environmental conditions and cold temperatures in the Antarctic meant that the data have a significantly lower signal to noise ratio than is usually attained from airborne hyperspectral sensors. We applied preprocessing techniques to improve the signal to noise ratio and convert the radiance images to ground leaving emissivity. Following preprocessing we developed and applied a fully automated processing chain to the hyperspectral imagery, which consists of the following six steps: (1) superpixel segmentation, (2) determine the number of endmembers, (3) extract endmembers from superpixels, (4) apply fully constrained linear unmixing, (5) generate a predictive classification map, and (6) auto-

Email address: martin.black@bas.ac.uk (Martin Black)

matically label the predictive classes to generate a lithological map. The results show that the image processing chain was successful, despite the low signal to noise ratio of the imagery; reconstruction of the hyperspectral image from the endmembers and their fractional abundances yielded a root mean square error of 0.58%. The results are encouraging with the thermal imagery allowing clear distinction between granitoid types. However, the distinction of fine grained, intermediate composition dykes is not possible due to the close geochemical similarity with the country rock.

Keywords: hyperspectral, thermal infrared, geology, automated, mapping, Antarctica

1. Introduction

Remote sensing in the solar reflective spectral range has been widely demonstrated to be an invaluable methodology to assist geological analysis (van der Meer et al., 2012). Hyperspectral data collected at visible and near infrared (VNIR; 0.4–1 µm) and shortwave infrared (SWIR; 1–2.5 µm) wavelengths have been widely reported in the literature for mapping mineral absorption features occurring within transition metals (i.e. Fe, Mn, Cu, Ni, Cr etc.) and alteration minerals that display absorption features associated with Mg-OH and Al-OH bonds (e.g. Abrams et al., 1977; Kruse et al., 1990; Hook and Rast, 1990; Hook et al., 1991; Clark et al., 1993; Kruse et al., 1993b; Abrams and Hook, 1995; Clark and Swayze, 1996; Resmini et al., 1997; Rowan et al., 2003).

Although these reflectance-based datasets have been successful for mapping of minerals associated with alteration, from a geological mapping perspective, mapping of rock-forming silicates is critical. When considering only VNIR/SWIR data there are significant limitations in the range and quality of the geological parameters that can be retrieved, as many important rock-forming minerals do not display diagnostic absorption features at VNIR/SWIR wavelengths (e.g. Drury, 2001; Gupta, 2003; van der Meer et al., 2012).

The longwave or thermal infrared (TIR; 8–14 µm) wavelength range has the capability of retrieving additional physical parameters and more accurately resolving the composition and physical condition of a material than solar reflected radiation (Hook et al., 1998, 2005; Hecker et al., 2012). Many common rock-forming minerals such as quartz, feldspars, olivines, pyroxenes, micas and clay minerals have spectral features in the 8-14 µm wavelength region (van der Meer et al., 2012). For silicate minerals, a pronounced emittance minimum caused by fundamental Si-O stretching vibrations occurs

near 10 μm (Hunt and Salisbury, 1975; Salisbury, 1991). The vibrational frequency, and thus the wavelength of the minimum, depends on the degree of coordination among the silicon-oxygen tetrahedra in the crystal lattice. Framework silicates, such as quartz and feldspar, have emittance minima at shorter wavelengths (9.3 and 10 μm, respectively) than do sheet silicates such as muscovite (10.3 μm) and chain silicates such as the amphibole minerals (10.7 μm) (Hunt, 1980). Emission Fourier transform infrared (FTIR) spectroscopy has been successfully used to predict modal mineralogy of rock-forming minerals such as feldspars, pyroxene, and quartz and their composition in igneous and metemorphic rocks (e.g. Feely and Christensen, 1999; Hamilton and Christensen, 2000; Milam et al., 2004; Hecker et al., 2010). Carbonates have features associated with CO_3 internal vibrations both in the 6-8 μm region (Adler and Kerr, 1963; Hunt and Salisbury, 1975) and also at 11.4 and 14.3 μm due to C-O bending modes. Sulphate minerals have an intense feature near 8.7 μm caused by fundamental stretching motions (van der Meer, 1995; Lane and Christensen, 1997).

The majority of geological mapping studies using thermal infrared remote sensing data have utilised multispectral data; multispectral sensors measure a small number of (< 20) broadly spaced, often non-contiguous bands (Kramer, 2002). The Advanced Spaceborne Thermal Emission and Reflection Radiometer (ASTER) and the Thermal Infrared Multispectral Scanner (TIMS) sensors have demonstrated the utility of TIR data to discriminate a wide range of minerals, especially silicates, as well as proving useful for lithological mapping (e.g. Rowan and Mars, 2003; Chen et al., 2007; Rogge et al., 2009; Haselwimmer et al., 2010, 2011; Salvatore et al., 2014); however, these satellite platforms are limited by their coarse spatial and spectral resolution.

The development of airborne hyperspectral TIR sensors producing images with tens to hundreds of contiguous spectral channels provided the potential for a step-change in the range of mineralogical information and accuracy of surface composition retrievable remotely. Currently, there are a number of operational airborne hyperspectral TIR instruments, including the Spatially Enhanced Broadband Array Spectrograph System (SEBASS), the Airborne Hyperspectral Scanner (AHS), the ITRES Thermal Airborne Spectrographic Imagery (TASI), and the Specim AisaOWL (van der Meer et al., 2012). Previous studies using airborne hyperspectral TIR data have illustrated the exceptional potential of these types of sensors for mapping silicates, carbonates, sulphates, and clays (e.g. Hewson et al., 2000; Cudahy et al., 2001; Calvin et al., 2001; Vaughan

et al., 2003, 2005; Aslett et al., 2008; Riley and Hecker, 2013; Kruse and McDowell, 2015).

However, a number of issues relating to processing of the imagery remain, which significantly affects the accuracy of the temperature-emissivity separation and subsequently the quality of the interpretation of the generated mineralogical and lithological maps. These issues include the coarser spectral resolution and poorer spectral calibration of currently available instruments (compared to VNIR/SWIR instruments), inaccurate correction of the effects of the atmosphere, low signal-to-noise ratios and a lack of understanding of the influence of a wide range of compositional, morphological, topographical and environmental factors on the spectral emissivity signal received at-sensor (Salvaggio and Miller, 2001; Shimoni et al., 2007; Feng et al., 2012). The complexity of the processing chain (atmospheric correction and the underdetermined nature of temperature emissivity separation; Gillespie et al., 1998) and lack of defined methodologies for processing of hyperspectral airborne TIR datasets relative to the processing of VNIR and SWIR hyperspectral datasets is an additional factor in limiting the usefulness of the data and the quality of geological interpretation (van der Meer et al., 2012).

A key objective of this study was to develop a fully automated processing chain, robust to noise, in order to produce a lithological map from airborne hyperspectral TIR data. The processing chain, with minimal inputs and parameters, is designed to assist geologists in processing, analysing and interpreting hyperspectral TIR datasets; we use established techniques which are routinely applied to VNIR/SWIR datasets and integrate them into a fully automated processing chain applied to hyperspectral TIR data.

Additionally, this paper also presents the first known analysis of airborne hyperspectral TIR data from the Antarctic.We tackle the significant challenges presented by the extreme environment in the Antarctic, which produced a dataset with a very low signal to noise ratio. The results are validated and interpreted in the context of the study area in conjunction with a full suite of ancillary data: detailed high quality ground reference spectral data collected using a new, high resolution field portable FTIR spectrometer, thin section and scanning electron microscope analysis, electron microprobe analysis, whole rock geochemical data and mineral modal analysis.

2. Study area and datasets

2.1. Study area and geological context

The Antarctic Peninsula is part of the proto-Pacific continental margin arc that was magmatically active at least from the Permain through to $\sim$ 20 Ma. The range of igneous rocks emplaced in continental margin arcs informs us about the tectonic history of the margin, and even relatively subtle difference between granitoid types (e.g. tonalite, diorite, granodiorite, granite) are significant as they record variations in melting depths and the stress regime in the lithosphere.

Anchorage Island is located in Ryder Bay to the south of the larger Adelaide Island, on the Antarctic Peninsula. The British Antarctic Survey (BAS) main research station is located close by on Rothera Point, Adelaide Island (Figure 1C). Anchorage Island was surveyed as part of a hyperspectral airborne campaign in February 2011 and visited for follow-up ground truth fieldwork in January/February 2014 (Figure 1D).

A local-scale geological map of the study area, based on previous geological mapping updated with recent field observations, is shown in Figure 2. The main geologic unit on Anchorage Island is the Adelaide Island Intrusive Suite (AIIS). The AIIS is dominated by granodiorites, tonalites and gabbroic rocks; granodiorite and hybrid gabbro/granodiorite plutons are the most abundant. The granodiorite is leucocratic and is dominated by plagioclase ($\sim$50–60 %), which often weathers orange/brown; quartz typically accounts for $\sim$10 % of the rock and K–feldspar $\sim$5 %. Mafic minerals are common (25 %), with green/brown amphibole abundant, along with minor amounts of biotite and epidote. The plutonic rocks are cut by dolerite and intermediate-felsic composition dykes, which are typically $<$ 1 m thick, dip steeply ($>$ 75° to the southeast) and strike in the range 210–230°.

2.2. Airborne hyperspectral data

Airborne hyperspectral TIR imagery was acquired on the 3rd February 2011 by the ITRES TASI sensor with 32 spectral bands from 8–11.4 µm at a full-width half-maximum (FWHM) of 109.5 nm. The acquisition system hardware and other equipment (inertial measurement unit and instrument control units) were installed into a De Havilland Twin Otter aircraft and flown unpressurised. Radiometric correction and geometric correction were carried out by ITRES Research Ltd., where a total of 17 flight lines were orthorectified and a mosaicked image in calibrated at-sensor radiance units

(Level 1B) at a ground spatial resolution of 1 m was delivered. The full preprocessing of the hyperspectral imagery is described in Section 3.3 and the automated lithological mapping in Section 3.4.

2.3. Field reflectance and emission spectral survey

Ground TIR emissivity spectra were acquired from the survey region during a field campaign in February 2014. A total of eight field localities were surveyed (Figure 1D) encompassing a northeast-southwest transect across Anchorage Island, though specific localities were selected due to their accessibility. At each locality, between 3 and 5 hand specimens were collected from representative lithological units, mafic enclaves and mineral viens (e.g. quartz) within close proximity ($<$10 m) of each field locality. Hand specimens were collected from weathered, nadir facing rock surfaces. Although varying levels of lichen cover were present, samples were measured from lichen-free (or minimal lichen covered) areas on each sample. Hand specimens were measured using an ABB full spectrum reflectometer (FSR) to gather measurements of spectral reflectivity and emissivity.

The FSR is a FTIR spectrometer which uses a Michelson interferometer (MB-3000) with mercury cadmium telluride (MCT) and indium arsenide (InAs) detectors. It has a wavelength range from 0.7–14 µm, a spectral resolution of $<$1 nm and a spot size of $\sim$4 mm. The FSR was developed by ABB for the Canadian Department for Research and Defence (DRDC). It represents a significant improvement over existing field FTIR spectrometers; it is compact and portable, has a high signal to noise ratio due do its cooled MCT and InAs detectors, as well as covering a large spectral range from the VNIR to TIR. The FSR is also a contact probe instrument, similar to spectral radiometers conventionally used for VNIR/SWIR spectroscopy. The spectral resolution was set to 0.1 nm and the instrument was set up such that each spectrum represented the average of 128 individual spectral measurements. A calibrated gold panel is built into the FSR allowing for the calculation of emissivity; the gold panel was used to recalibrate the instrument at the start of each batch of measurements at each field locality. Figure 3 shows 18 spectra collected from exposed nadir facing samples (excluding samples from enclaves or vein material).

3. Methodology

The processing of the airborne hyperspectral TIR imagery was split into two main phases; (1) data preprocessing and (2) fully automated image processing and lithological mapping. To assist in the analysis of the results from the airborne remote sensing study a comprehensive field mapping survey was carried out supported by field reflectance and emission spectroscopy (Section 2.3). The field spectral data underwent spectral resampling (Section 3.1). Laboratory geochemical and petrographic analyses were carried out to determine mineralogical information and aid in interpretation of field spectral data (Section 3.2).

3.1. Spectral resampling

All of the emissivity spectra collected in the field (Figure 3) using FSR were convolved to the spectral response functions of the TASI sensor through

$$\varepsilon_i = \frac{\int \varepsilon_s(\lambda) r_i(\lambda) \delta\lambda}{\int r_i(\lambda) \delta\lambda} \tag{1}$$

where ε_i is convolved emissivity, $\varepsilon_s(\lambda)$ is the sample's emissivity at band i and wavelength λ, $r_i(\lambda)$ is the spectral response function of band i at wavelength λ_j, over the wavelength interval of the sample $\delta\lambda$.

3.2. Geochemical and petrographic analyses

Four samples representative of the main lithological units (granite, granodiorite and dolerite) were further investigated to understand their geochemistry; two granodiorite samples (J13.19.10 and J13.22.5), one granite (J13.21.10) and one dolerite sample (J13.22.10) were chosen. These samples were selected to ensure that each of the geological units on Anchorage Island were investigated; as weathered granodiorite represents the major lithological unit on Anchorage Island, two weathered granodiorite samples were chosen to determine their homogeneity. Thin sections were examined using a petrological microscope, a FEI Quanta 650F QEMSCAN scanning electron microscope and a Cameca SX-100 electron microprobe. Backscattered electron (BSE) images were collected on the QEMSCAN using an accelerating voltage of 20 kV and a working distance of $\sim$ 13 mm. Major element geochemistry and the identification of minerals and mineral phases was carried out through electron microprobe anaysis

(EPMA) of points ($\sim$ 5 µm) from grains within thin sections. Point counting (Galehouse, 1971) was used to determine mineral composition; 500 points were counted in thin section on each of the four samples.

The samples were also analysed by X-ray fluorescence spectrometry (XRF) to determine whole-rock major and trace elements using a PANalytical Axios-Advanced XRF spectrometer at the University of Leicester. Powders from whole-rock samples were obtained through crushing in a steel jaw crusher and powdering in an agate ball mill. Major elements were determined from fused glass discs and trace elements from powder pellets. Loss on ignition (LOI) values were calculated by igniting $\sim$3 g of each sample in ceramic crucibles at 950 °C. Glass discs were prepared from 0.6 g of non-ignited powder and 3 g of lithium metaborate flux, melted in a Pt-Au crucible over a Spartan burner then cast into a Pt-Au mould. Powder pellets of 32 mm diameter were produced from mixing 7 g of fine ground sample powder with 12-15 drops of a 7% polyvinyl alcohol (PVA) solution (Moviol 8-88) and pressed at 10 tons per square inch.

3.3. Hyperspectral data preprocessing

Figure 4 shows a flowchart of the preprocessing steps. Radiometric correction and geometric correction were carried out by ITRES Research Ltd. using their proprietary tools. In the first step, radiometric and spectral calibration coefficients were applied to convert the raw digital numbers into spectral radiance values. In the second step, the ITRES proprietary geometric correction software utilised the navigation solution, bundle adjustment parameters, and digital elevation models (DEMs) to produce georeferenced radiance image files for each flight line. In addition, flight lines were combined into an image mosaic of the area. The nearest neighbour algorithm was used to populate the image pixels so that radiometric integrity of the pixels could be preserved. Where the pixels of adjacent flight lines overlapped the pixel with the smallest off-nadir angle was written to the final mosaic image.

Whilst the TIR domain is an atmospheric window, there is atmospheric influence which needs to be compensated for, especially for quantitative applications (Liang et al., 2002). Here we performed atmospheric correction through the inversion of radiative transfer modelling, following a similar approach to our corrections of VNIR/SWIR Antarctic hyperspectral data (Black et al., 2014).

The basic radiative transfer equation in the TIR domain as given by Dash et al. (2002) is (where each term is a function of wavelength, λ, omitted for clarity)

$$L_s = L_p + \tau \cdot L_g + \tau \cdot [1 - \varepsilon] \cdot \frac{F}{\pi} \quad (2)$$

where L_s is the total thermal radiance received at-sensor, L_p the thermal path radiance emitted by the atmosphere between the ground and the sensor, τ the ground-to-sensor transmittance, L_g the ground emitted radiance, ε the ground surface emissivity and F the downwelling thermal sky flux at the ground (Richter and Coll, 2002). We utilised ATCOR-4 (Richter and Schläpfer, 2002, 2014) to perform atmospheric correction; ATCOR-4 applies equation 2 by interpolating the required atmospheric parameters for each pixel based on their individual viewing geometry where the radiative transfer parameters are selected from a database of MODTRAN-5 (Berk et al., 2005) simulations. The two inputs required by ATCOR-4 to approximate the atmospheric conditions are the visibility and column water vapour amount. Visibility data is continually measured at the nearby Rothera research station using an automated BIRAL HSS VPF-730 Combined Visibility & Present Weather Sensor. The water vapour value was derived using an assumed value of 2.0 $g\,cm^{-3}$ by comparison to radiosonde data. The mosaicked image was processed one flight line at a time to convert the at-sensor non-atmospherically corrected radiance into ground-leaving radiance. Temperature and emissivity separation (TES) was performed following atmospheric correction using the maximum-minimum difference of emissivity technique, which is commonly applied to ASTER TIR data (Gillespie et al., 1998).

Investigation of the emissivity imagery following atmospheric correction and TES showed lower than expected emissivity values, along with residual atmospheric absorptions. This was likely due to the challenging acquisition conditions and calibration conditions of the instrument, along with inadequate representation of the atmosphere due to the approximations in the atmospheric correction process (Black et al., 2014). An empirical correction, through the Emissive Empirical Line Method (EELM; Distasio Jr. and Resmini, 2010) was applied. The EELM generates scalar multiplicative values for each band of the image through regression of image pixel spectra to the assumed "target" spectra - this approach is comparable to the use of pseudo invariant features (PIFs; Freemantle et al., 1992; Philpot and Ansty, 2011) and the empirical line method (ELM; Smith and Milton, 1999) which is commonly applied to VNIR/SWIR data (*e.g.* Tuominen and Lipping, 2011). Here we applied EELM utilising pixels selected from homogeneous regions of granite, dolerite, snow and sea water.

High levels of salt and pepper noise along with within-in track striping and flight line illumination differences were still apparent in emissivity imagery so an additional processing step was applied to improve the signal-to-noise ratio (SNR). The minimum noise fraction (MNF; Boardman and Kruse, 1994; Green et al., 1998) was applied. The MNF involves two cascaded principal component (PC) transformations; the first transformation, based on an estimated noise covariance matrix, decorrelates and rescales the noise in the data. The second step is a standard PC transformation of the noise-reduced data. The MNF is an effective technique for reducing a large hyperspectral dataset into fewer components which contain the majority of information (spectral variance) in a small number of components. Unlike a PC transform, the resulting axes (components) from MNF are not orthogonal (as in PC analysis) but are ordered by decreasing signal to noise ratio (Keshava and Mustard, 2002). After the MNF was applied, the first four MNF bands were then used in the inverse MNF to produce the noise-reduced emissivity image. Additionally a median filter with a radius of 2 was applied in the spectral domain to remove shot noise which was not addressed by the MNF noise reduction step (*e.g.* Gilmore et al., 2011).

We investigated the SNR of the image before and after preprocessing by utilising an area of sea water in the image and calculating the SNR through

$$\mathrm{SNR} = \frac{\mu_{ij}}{\sigma_{ij}} \tag{3}$$

where i and j are the rows and columns of the image, μ_{ij} is the mean of the pixels and σ_{ij} is the standard deviation of the pixels. The signal to noise ratio is often reported using the logarithmic decibel (dB) scale; we can express the SNR in dB through

$$\mathrm{SNR}_{dB} = 20\log_{10}(\mathrm{SNR}) \tag{4}$$

Finally, prior to processing, the image was masked to remove snow/ice and sea water. The mask was generated from the temperature image where pixels < 5 °C were removed.

3.4. Image processing and lithological mapping

In order to produce a lithological map, we applied a six step processing chain, shown in Figure 5. The processing chain is fully automated, with only a small num-

ber of inputs/parameters; algorithms were selected from the existing literature based on their ability to cope with low SNR datasets. The six steps are: (1) superpixel segmentation; (2) identify the number of endmembers to extract from the superpixels; (3) extract endmembers from the image using an endmember extraction algorithm (EEA); (4) perform spectral mixture analysis (SMA; also known as spectral unmixing) to determine the fractional abundances each endmember; (5) produce a predictive classification map from endmember fractional abundances; (6) identify endmembers and label the predictive map classes to produce a lithological map.

Here we consider an endmember to be a unique spectrum derived from the hyperspectral scene itself. Endmembers are found directly from the image, regardless of the composition of materials (within individual pixels or within the scene itself) or any imperfections in the dataset (e.g. sensor noise, atmospheric influence and so on) (Winter, 1999). Through the careful interpretation of endmembers in reference to the local geological context, ancillary data (e.g. geochemical analysis) and knowledge of the imperfections within the data, endmembers which are *recognisable* are determined and interpreted in a geological context (Winter, 1999; Rogge et al., 2009).

These steps are fully automated in a MATLAB environment (MathWorks, 2011) and do not require any user interaction. Steps 1 to 5 require the hyperspectral scene and few parameters as input. In this study, we also perform step 6 automatically with the additional input of the field spectral data (convolved to TASI spectral response functions; Equation 1), which are used to automatically label the predictive map classes. In the absence of field spectral data, step 6 could be performed through manual interpretation of endmembers and subsequent labelling of the predictive map classes by an expert user. Due to the automated nature of the processing chain, the results are also completely repeatable unlike approaches which rely on manual endmember identification. The following sections describe each step of the processing chain.

3.4.1. Step 1: Superpixel segmentation

Firstly, we apply superpixel segmentation, which adds a spatial component to endmember extraction. Superpixels are homogeneous image regions comprised of several pixels having similar values and are generated by intentional over-segmentation of the emissivity image which aggregates scene features into segments (Thompson et al., 2010; Gilmore et al., 2011); the spectra of each of the original image pixels within a superpixel segment are averaged to produce the superpixel's spectrum.

Briefly, the superpixel segmentation uses graph-based image segmentation (Felzenszwalb and Huttenlocher, 2004), where the pixel grid is shattered into an 8-connected graph with nodes connected by arcs representing the Euclidean spectral distance and the nodes are then iteratively joined using an agglomerative clustering algorithm (Felzenszwalb and Huttenlocher, 2004; Thompson et al., 2010, 2013). A stable bias parameter, k controls the size of the superpixels, a minimum superpixel size is enforced, and in a final step smaller regions are merged to their nearest adjacent clusters (Felzenszwalb and Huttenlocher, 2004; Thompson et al., 2010). The superpixel approach has been shown to be beneficial on low SNR datasets and can aid in deriving endmembers that more closely resemble manually derived endmembers (Thompson et al., 2010). This is due to averaging several pixel spectra within a single superpixel and thus the technique reduces the noise variance proportionally to the superpixel area. However the technique can act to degrade spectral purity by aggregating multiple pixels and can suppress subtle spectral features (Thompson et al., 2010).

For the superpixel segmentation we set the bias parameter k to 0.1 and the minimum superpixel region size to 30 pixels using the Euclidean spectral distance as the divergence measure. These parameters were determined quantitatively by investigating the sensitivity of the segmentation to small features, such as the stoped granite block in the northeast of Anchorage Island (Figure 2). These parameters are determined based on the scale of features present in the scene and the spatial resolution of the imagery, thus may require local tuning on other imagery collected at different resolutions or where geological features occur at different scales. The superpixel segmentation step also serves as an image reduction step, thereby speeding up processing times; the raw image contains over 7.6 million pixels (3062×2489) and the superpixel segmentation reduces this to 9810 superpixels.

3.4.2. Step 2: Estimating the number of endmembers

Following the generation of superpixels, Virtual Dimensionality (VD; Chang and Du, 2004) was used to determine the number of endmembers (n). The number of endmembers, or the intrinsic dimensionality (ID) of a hyperspectral image is considerably smaller than the component dimensionality (number of bands), and accurately determining the ID is crucial for the success of endmember extraction and spectral mixture analysis (Chang and Du, 2004). The high spatial and spectral resolution of hyperspectral imagery means that the sensor is capable of uncovering many unknown endmem-

bers, which cannot be identified by visual inspection or known *a priori* (Chang and Du, 2004). In order to determine the number of endmembers (or signal sources, i.e. the intrinsic dimensionality) we applied the VD algorithm, prior to endmember extraction. The VD concept formulates the issue of whether a distinct signature is present or not in each of the spectral bands as a binary hypothesis testing problem, where a Newman-Pearson detector is generated to serve as a decision-maker based on a prescribed false alarm probability P_{fa} (Chang and Du, 2004; Plaza et al., 2011). In our preliminary investigations, we varied the P_{fa} from 10^{-3} to 10^{-6}, however, the estimated number of endmembers did not change; we therefore fixed the P_{fa} value to 10^{-4} in line with previous studies (Chang and Du, 2004; Plaza et al., 2011).

3.4.3. Step 3: Endmember extraction

In step (3) we applied Vertex Component Analysis (VCA; Nascimento and Bioucas-Dias, 2005), to extract *n* endmembers from the superpixels. Vertex component analysis exploits the fact that endmembers occupy the vertices of a simplex and assumes the presence of pure pixels in the data. The algorithm iteratively projects data onto a direction orthogonal to the subspace spanned by the endmembers already determined and the new endmember signature corresponds to the extreme of the projection; iteration continues until the number of endmembers is exhausted. The algorithm has been shown to be comparable to state of the art endmember extraction algorithms, such as N-FINDR (Winter, 1999) and outperforms manual techniques such as the Pixel Purity Index (PPI; Boardman, 1993). It is an order of magnitude less computationally complex than other state of the art endmember extraction algorithms which yields significantly faster processing times for large datasets (Nascimento and Bioucas-Dias, 2005).

3.4.4. Step 4: Spectral mixture analysis

The endmembers derived from the VCA algorithm were used as input to step (4) where linear SMA is used to produce fractional abundances of the *n* endmembers using the original image (without superpixel segmentation). Due to its ease of implementation, we applied fully constrained linear spectral unmixing (FCLSU; Heinz and Chang, 2001) to derive fractional abundances of each endmember, given as

$$R_b = \sum_{i=1}^{n} F_i S_{ib} \tag{5}$$

where R_b is the fractional abundance of the pixel at band b, F_i is the fractional abundance of endmember i, S_{ib} describes the emissivity of endmember i at band b, and n is the number of endmembers. Equation 5 was solved subject to the constraints that fractional abundances sum-to-one (ASC; abundances sum-to-one constraint) and fractional abundances are non-negative (ANC; abundance non-negative constraint) (e.g. Rogge et al., 2009). This step results in fractional abundance images, where, for each pixel in the image, the abundance of each endmember is determined. The algorithms used at this and the preceding processing steps were selected due to their availability and implementation in the MATLAB environment (MathWorks, 2011), along with their relatively quick processing times and proven success at extracting endmembers under moderate to high noise conditions (Nascimento and Bioucas-Dias, 2005; Chang and Plaza, 2006; Plaza et al., 2012).

3.4.5. Step 5: Predictive map classification

Utilising the abundance images a predictive classification map was generated following a similar approach to Rogge et al. (2009). The map was generated by determining the endmember with the maximum fractional abundance for each pixel and assigning that pixel to the given endmember class. For a pixel to be assigned to a particular class, the endmember abundance must be above a minimum fractional abundance threshold (or confidence level), otherwise a null class was assigned. The minimum fractional abundance was set to the intermediate value of 0.5 for practical purposes, however this value could be increased to identify spectrally purer regions (Rogge et al., 2009).

3.4.6. Step 6: Class labelling

The interpretation step was carried out to produce geological labels which were automatically applied to the classification map generated from step (5). The image derived endmember spectra were compared to field emissivity spectra (*e.g.* Harris et al., 2005; Rogge et al., 2009) through calculation of spectral angle (SA), also known as Spectral Angle Mapper (SAM; Kruse et al., 1993a) through the application of

$$\mathrm{SA} = cos^{-1}\left(\frac{\vec{t}\cdot\vec{r}}{\|\vec{t}\,\|\cdot\|\vec{r}\,\|}\right) \tag{6}$$

where t represents the spectrum of the target (endmember), r represents the spectrum of the reference (field spectra) and SA is the spectral angle (in radians; 0 to 2π). This

technique to determine similarity is insensitive to gain factors as the angle between two vectors is invariant with respect to the lengths of the vectors, and allows for laboratory spectra to be directly compared to remotely sensed spectra (Kruse et al., 1993a). Predictive map classes were automatically labelled by their closest match from the field spectral data (*e.g.* Rivard et al., 2009).

3.5. Image processing validation

In order to validate our findings, we use the root mean square error metric (RMSE) for assessment (e.g. Plaza et al., 2012). We define $\hat{y}_{ij}$ as the reconstructed hyperspectral image, following

$$\hat{y}_{ij} = \sum_{n=1}^{n} (M_n \times S_n) \tag{7}$$

where i and j are the rows and columns of the image, n is the number of endmembers, M_n denotes the endmember spectrum of n and S_n denotes the fractional abundance of endmember n. Following this reconstruction we calculate the RMSE between the original hyperspectral image, y and the reconstructed hyperspectral image, $\hat{y}$ as

$$\mathrm{RMSE}(y,\hat{y}) = \left(\frac{1}{B} \sum_{j=1}^{B} [y_{ij} - \hat{y}_{ij}]^2 \right)^{\frac{1}{2}} \tag{8}$$

where B is the number of spectral bands and $\hat{y}_{ij}$ and y_{ij} are pixels of the original hyperspectral image and the pixels of the reconstructed hyperspectral image respectively. Summary statistics were calculated from the RMSE of the pixels of each endmember class as well as the whole RMSE image.

Additionally, we also extract the original image spectra and the reconstructed image spectra (calculated from the endmembers and their fractional abundances). Using areas of granite and granodiorite we extract spectra from pixels of high purity (0.9 fractional abundance), medium purity (0.75 fractional abundance) and low purity (0.5 fractional abundance) and compare the spectra, their fractional abundances, and the RMSE values to validate the findings in a spectral context.

4. Results and Discussion

4.1. Field data

Table 1 shows whole-rock major and trace element data from XRF spectroscopy. Table 2 shows the abundances of minerals as determined from point counting. Spectral

data collected from in situ samples is displayed in Figure 3. The majority of Anchorage Island is composed of weathered granodiorite, however some areas contain amphibole rich granodiorites (J13.24, J13.25 and J13.26), and areas in the southwest of the island display strongly weathered and altered granodiorites (J13.19 and J13.20).

The spectral variability of the granidiorites is shown in Figure 3A. Numerous dolorite dykes cut the granodiorite unit; a spectral measurement from a dolerite dyke in the northwest of Anchorage Island is shown in Figure 3B. The field spectra for dolerite and granodiorite show similar spectral features; a small relative increase in emissivity at 8.6 μm and 9.5 μm, and two broad flat absorption features centred around 9 μm and 10 μm. The whole-rock XRF data shown in Table 1 support the spectral similarity of the dolerite and granodiorite samples - there is very little difference in the chemical composition of these samples, hence the similar spectra of the samples. The amphibole rich granodiorite spectra display an additional weak feature at 10 μm with reduced magnitude of the emissivity maximum at 8.6 μm. The strongly weathered (and altered) granodiorite spectra are significantly different to weathered/amphibole rich granodiorite spectra, displaying a broad deep feature at 9 μm and a smooth spectrum above 9.8 μm. We attribute the broad deep absorption centred around 9 μm to high temperature feldspar alteration into clay minerals (e.g. sericite).

The spectrum of granite is dominated by a quartz signal which leads to an emissivity maximum at 8.7 μm and a deep feature with an emissivity minimum at 9.4 μm (Figure 3B). Although similar spectral features to granodiorite are present in the granites, the overall magnitude of the absorption features in much larger in the granite than in any of the granodiorite or dolerite spectra.

4.2. TIR data preprocessing results

Figure 6 shows the first 10 bands of the MNF transform. As higher MNF components are considered, the levels of noise dramatically increase (Figure 6G-J). The MNF images also clearly highlight the differences between flight lines which cause ‘striping‘ in the images (e.g. Figure 6E and F). The first four of these MNF components (Figure 6A-D) were retained and processed through an inverse MNF transform prior to input in the superpixel and endmember extraction algorithms.

Figure 7 shows the SNR for the image after atmospheric correction and TES compared to the SNR for the final image after all preprocessing (atmospheric correction, TES, EELM and MNF noise reduction). Overall the SNR is increased from a mean

value of 60:1 (35.6 dB) to 92:1 (39.3 dB) after preprocessing. With the exception of one band at $\sim$ 9 µm, the SNR increased for all wavelengths, with significant increases seen at the higher wavelengths ($>$ 10.5 µm). Whilst increases in SNR are seen after preprocessing, on whole SNR values are relatively low and far lower than that which are regularly reported by others using airborne hyperspectral TIR sensors such as SEBASS; for example Vaughan et al. (2003) report SNR values of 2000:1 (66 dB) using SEBASS data in Nevada.

The low SNR values reported here are likely a direct result of the challenging operating conditions in the Antarctic; the instruments were flown in an unpressurised aircraft, operating at extreme temperatures which were up to 20 °C (68 °F) outside of the instrument's normal operating range, as well as being subject to repeated heating and cooling cycles during storage and operation (Black et al., 2014).

4.3. Predictive map generation and geological interpretations

A total of 9810 superpixels were input into the VD algorithm which determined there were 5 endmembers. The endmembers were extracted using the VCA algorithm and are shown in Figure 8. Endmember abundances were determined using FCLSU; the abundances images were utilised to generate a classified map, where classes were assigned to the predominant endmember if the abundance was greater than 0.5.

The classes were subsequently labelled by automatic matching to the field spectral data; the closest match (in terms of spectral angle; Equation 6) was applied to label the endmembers (Figure 8) and their respective class in the predictive classification map (Figure 9). The results were validated through visual inspection of the classification map with respect to the local geological map (Figure 2), comparison of the endmember spectra and the ancillary data (Sections 2.3 and 3.2), as well as using the RMSE metric (Section 3.5 and Section 4.4). Endmember-4 was excluded as it represented sea water from pixels which were not captured at the masking step and is not discussed further. The resulting lithological map is shown in Figure 9.

For each endmember, a match was determined from the field spectra where the SA was $\leqslant$ 0.03 radians; we found confident matches for granite, two types of weathered granodiorite and altered granodiorite. The endmember spectra display absorption features consistent with the field measured spectra (Figure 3) and their mapped distributions (Figure 9) are largely in agreement with the generalised geological map (Figure 2).

The granite endmember (Endmember-1; Figure 8A) displays good agreement with the field spectral data and its distribution on the predictive map (Figure 9A and B). We accurately delineate the stoped granite block in the northeast of Anchorage Island, along with the larger outcrops south of the granite block and along the northeast coast. The predictive map indicates the likelihood of additional outcrops of granite occurring predominantly in the northeast of Anchorage Island (Figure 9B).

The occurrence of granite *senso stricto* in continental margin arcs is rare, typically accounting for 1-2% of the total volume of granitoid rocks exposed at the surface. Granites exposed at the surface on the western margin of the Antarctic Peninsula are rare and not previously identified at all from Adelaide Island (or the Ryder Bay islands, including Anchorage Island, prior to mapping carried out in this study). The identification of stoped blocks of granite within a granodiorite pluton indicates the presence of granite at relatively shallow depths.

Two of the endmembers (Endmember-2 and Endmember-3; Figure 8B and C) show good matches to granodiorite spectra measured in the field; both are measured from weathered granodiorite, however Endmember-3 is from yellow/orange weathered granodiorite. The spatial distribution of this endmember is largely limited to low lying coastal regions, perhaps indicating recent weathering due to coastal processes, which distinguishes it from the remaining granodiorite (Endmember-2). Endmember-3 also shows a higher abundance in the extreme southwest of Anchorage Island, corresponding to the diorite outcrop (c.f. Figure 2), though does not allow for distinguishing the diorite as a separate unit; this is likely as the diorite and granodiorite units would have a similar chemical composition and thus would be difficult to differentiate spectrally. Endmember-5 shows a good agreement with a measured spectrum from the strongly altered granodiorite (Figure 8D), with a deep emissivity feature centred at 9 μm, however there are additional features located at 10 and 11 μm which are not seen in the field spectrum. Endmember-5 is largely distributed proximal to, or within the larger spatial lithological unit of the granodiorite (Endmember-2) and is distinct from the granite unit (Endmember-1). The yellow/orange weathered and altered grandiorites (Endmember-3 and Endmember-5 respectively) have their greatest abundance in the central southwest region of the Island (concurring with the field observations; Section 4.1).

None of the endmembers correspond to the dolerite, most likely due to the chemical and spectral similarity to the granodiorite unit (Table 1; Figure 3). The granodiorite

and dolerite were distinguished in the field due to the differences in their grain size; however, the spectral features present in the imagery do not allow for a distinction to be made. Even in the field spectra, there is little difference between the granodiorite and dolerite (Figure 3), hence there are no endmembers extracted that match dolerite.

At the wavelengths considered by the TASI sensor (8 to 11.5 μm), we have been able to differentiate granite and granodiorite, whilst struggled to find a clear distinction between the relatively similar chemical composition of the country rock (granodiorite) and the dolerite dykes on Anchorage Island. The ability to more accurately discriminate potassium and plagioclase feldspar(s) could be possible if data were available at wavelengths where additional features could aid in feldspar discrimination (e.g. 12-14 μm; Hecker et al., 2012).

4.4. Validation of image processing

Figure 10 shows the RMSE histogram and image calculated through Equation 8. Summary statistics calculated for each of the predicated class pixels (Figure 9) within the RMSE image are shown in Table 3.

Endmembers 1, 2 and 5 produce RMSE values of $<0.5\%$, with standard deviations of $\sim 0.45\%$ and a maximum RMSE of 7.83% (Endmember-1). These values indicate that the unmixing procedure with just 5 endmember spectra yielded a high quality reconstruction of the original image spectra for these classes. Endmember-3 has a mean RMSE which is significantly higher at 0.94% with an increased standard deviation of 1.25% and a maximum error of 23%; this indicates pixels which are classed as Endmember-3 have higher overall and specific reconstruction errors, likely a result of incorrect or inadequate endmember spectra for these pixels and hence higher errors.

On the whole, the average RMSE for the image is 0.58%; this figure is significantly higher than the RMSE values that are routinely achieved using VCA (e.g. RMSE of 0.1% in Plaza et al., 2012), however this is likely a direct result of the low SNR of the imagery (Figure 7). As the SNR is reduced (below 1000:1, 60 dB) the performance of endmember extraction algorithms begins to degrade significantly and RMSE values increase (Plaza et al., 2012). Conversely, with larger SNRs, the RMSE error will decrease and the performance of endmember extraction algorithms will improve (Nascimento and Bioucas-Dias, 2005; Plaza et al., 2012). Other factors may also affect the RMSE values, including the pure pixel assumption and spectral mixture analysis

techniques, as discussed in Section 4.5. However, these errors did not inhibit the success of the processing chain.

Figure 11 shows the spectra of pixels from high, medium and low purity pixels, comparing the original image spectra with the reconstructed image spectra (from endmembers and their fractional abundances), for granite, granodiorite and altered granodiorite. In all cases the RMSE is $\leqslant 2$ %, indicating a good fit between the original and reconstructed spectra. The high purity pixels (Figure 11A) more closely resemble the original endmembers and their equivalent field spectra (c.f. Figure 8), indicating a good degree of reconstruction of the original spectra and that endmember lithologies are accurately represented. When considering the medium and low purity spectra (Figure 11B and C), the RMSE values are still low, indicating a high degree of fit between the original and reconstructed spectra; however, as the mixing of endmembers is increased, the pixel spectra begin converge and become increasingly similar (especially at low purities, Figure 11C). This indicates that as pixels become increasingly mixed (lower fractional abundances) the pixel spectra are similar yielding lower confidence in assigning a distinct lithology for low purity pixels. In this study we defined our abundance threshold at 0.5, however with careful examination of reconstructed and original image spectra, this threshold value could be increased to yield greater confidence in lithological units (as pixel spectra would more closely resemble endmember spectra).

4.5. Processing chain and algorithm considerations

Here we considered a pure pixel scenario, the assumption that at least one 'pixel' contains a pure endmember spectrum. We note that a pure endmember spectrum represents an independent signal source in the image and in some cases is not necessarily a geologically meaningful (or interpretable) spectrum; for example some endmember spectra could be related to image noise or atmospheric effects (Winter, 1999). However, processing hyperspectral imagery assuming a pure pixel scenario has been widely researched, with a variety of pure pixel techniques for each step of the processing chain along with the optimised implementation and proven success of published algorithms. The pure pixel approach has been successful when images contain pure pixels (Plaza et al., 2012); however, given the presence of the mixing at different scales (even at microscopic levels), the pure pixel assumption is not always true, as some images may only contain pixels which are completely mixed (Plaza et al., 2012).

The complexity of endmember extraction from hyperspectral imagery is increased in a mixed pixel scenario, since the endmembers, or at least some of them, are not in the image (Bioucas-Dias, 2009). We note a point for future research into mixed pixel endmember extraction techniques which follow from the seminal ideas of Craig (1994), based on the minimum volume transform, with a number of recently published algorithms building from this work (Berman et al., 2004; Miao and Qi, 2007; Li and Bioucas-Dias, 2008; Chan et al., 2009; Bioucas-Dias, 2009). Currently, the major shortcoming of mixed-pixel techniques is long processing times due to their computational complexity (Bioucas-Dias, 2009). However mixed pixel techniques are an active area of research and as the algorithms mature they should be integrated into future studies. Additionally, the long established pure pixel methods should not yet be discounted; technological advances such as miniaturisation of sensors will inevitably lead to very high spatial resolution as sensors are deployed from platforms such as Unmanned Aerial Vehicles (UAVs).

For SMA, also known as spectral unmixing, we considered the fully constrained linear model due to its ease of implementation and flexibility in different applications (Chang, 2003). We have not considered linear unmixing using iterative spectral mixture analysis (ISMA; Rogge and Rivard, 2006), which seeks to minimise the error by unmixing on a per pixel basis using optimised endmember sets. Alternatively, non-linear SMA may best characterize the resultant mixed spectra for certain endmember distributions, such as those in which the endmember components are intimately mixed (Guilfoyle et al., 2001; Plaza et al., 2009). In those cases, the mixed spectra collected at the imaging instrument are better described by assuming that part of the source radiation has undergone multiple scattering prior to being measured at the sensor.

In a non-linear model, the interaction between the endmembers and their fractional abundance is given by a non-linear function, which is not known *a priori*. Various techniques have been proposed in the field of machine learning, with neural networks some of first non-linear SMA approaches proposed (Benediktsson et al., 1990). The performance of non-linear SMA algorithms on large, real-world hyperspectral data is currently limited by the computational complexity of the techniques; however, recent advances have aimed to take advantage of parallel processing techniques to reduce computational time (e.g. Plaza et al., 2008) and such algorithms remain an area for future research as their implementations become publicly available.

4.6. *Future applicability of the processing chain*

The processing chain presented here is fully automated and repeatable; after pre-processing, the six step processing chain is fully automated, using few inputs and parameters, followed by predictive map generation and automatic class labelling using the field spectral data. This is a direct attempt to address the current paucity of such automated approaches in the geological remote sensing community (van der Meer et al., 2012). We anticipate the technique could be applied by geologists without the need for 'expert' remote sensing knowledge or complicated image processing techniques / software packages, and the processing chain is more automated and less manually involved than traditional techniques. Indeed, this processing chain is particularly advantageous in the polar regions where higher detail lithological mapping can be obtained using remote sensing than compared with traditional field mapping.

The main parameters which affect the lithological mapping processing chain are the superpixel bias parameter and minimum size segment size. The parameters are discussed and explained in detail by Thompson et al. (2010). The bias and minimum size segment size parameters control the size of the superpixels and should be scaled appropriately depending on the features of interest in each particular scene. The parameters used in this study were quantitatively determined by inspecting the superpixel segmentation image and considering the scale of the geological areas of interest (e.g. dykes), however these parameters would require local tuning for other study areas, and particularly for other scales and image resolution (such as coarser resolution satellite imagery). The abundance threshold can be tuned to extract purer regions, however we demonstrate the results here using a moderate threshold of 0.5; higher values would yield spectrally purer regions (e.g. Rogge et al., 2009).

We have achieved the results presented here in spite of what might be described as 'extremely high noise conditions' (SNR $\leqslant$ 40 dB; Plaza et al., 2012), thereby serving as a validation of the processing chain and its ability to operate effectively at low SNR values. We confirm the findings of the Thompson et al. (2010) and Gilmore et al. (2011), such that superpixel segmentation aids in the determination of *recognisable* endmembers which are interpretable in a geological context despite low SNR values. Such a finding is crucial for future studies in the Antarctic where the environmental conditions mean that achieving high SNR values is much more challenging compared with temperate parts of the world. Indeed, this finding is also advantageous for many

studies, not just the Antarctic, where challenging conditions can yield lower than expected SNRs; hence, it is advantageous that the processing chain can yield successful results even at low SNRs.

It is an important point to note for future applications that prior knowledge of the local geology (and/or vegetation) is required for the successful application of the processing chain. The identification of the image derived endmembers (step 6) was successful here, in large part due to availability of high quality field spectral measurements to allow for comparison along with ancillary data (geochemical analysis). However, in lieu of field spectral measurements, a user could produce geological interpretations with knowledge of the local geological context, an understanding of the imperfections in the hyperspectral imagery (e.g. residual noise due to inadequate atmospheric compensation) and the identification of endmembers could be aided through comparison to spectral libraries (e.g. Christensen et al., 2000).

The techniques presented here could be easily transferred to other TIR data (or even VNIR/SWIR data), including currently available satellite data, such as ASTER, or even planned future satellite TIR data; for example, the HyspIRI satellite has a planned TIR instrument which includes 7 bands in the 7-13 μm spectral range (Hulley et al., 2012). The coarser spatial and spectral resolution of this data would yield difficulties in the exact identification of minerals, though previous TIR data, such as ASTER, has been used to reliably discriminate a wide range of minerals, especially silicates, as well as proving useful for lithological mapping (e.g. Rowan and Mars, 2003; Chen et al., 2007; Rogge et al., 2009; Haselwimmer et al., 2010, 2011; Salvatore et al., 2014). Additionally, technological advances and increasing miniaturisation will eventually lead to the availability of UAV-deployable research grade hyperspectral sensors which could be used operationally by field geologists as a tool to compliment traditional field mapping techniques. The use of an automated processing chain in such a situation would be highly advantageous in delivering fast, automated and repeatable lithological mapping results which could aid and inform traditional mapping approaches operationally in the field.

5. Conclusion

We have presented a fully automated processing chain to produce lithological maps using airborne hyperspectral thermal infrared data in spite of low signal to noise ratios.

We utilised an airborne hyperspectral TIR dataset, collected for the first time from Antarctica, to accurately discriminate grantoids. The challenging conditions and cold temperatures in the Antarctic yielded data with a significantly lower SNR compared with data collected in more temperate environments. As a result, several preprocessing steps were employed to refine the imagery prior to analysis; atmospheric correction and temperature emissivity separation were applied, followed by further empirical corrections and noise removal through the minimum noise fraction technique. Areas of snow and sea water were subsequently masked using the temperature image.

The processing chain was established and applied to the preprocessed imagery. Firstly, superpixel segmentation was applied to aggregate homogeneous image regions comprised of several pixels having similar values into larger segments (superpixels). The superpixels were input into the VD algorithm to determine the number of endmembers, which were subsequently extracted using VCA and unmixed using FCLSU to generate abundances of each endmember. A predictive classification map was created where endmember fractions were thresholded (> 0.5). The endmembers extracted were automatically matched to their closest spectrum from the field spectral data, and the observations made in the field from these measurements were used to label the predictive map classes and generate a lithological map.

The fully automated processing chain was successful in identifying 4 geologically interpretable endmembers from the study area. Reconstruction of the hyperspectral image from the endmembers and their fractional abundances yielded a root mean square error (RMSE) of 0.58%. The RMSE value, almost twice as large as previous studies, is likely a result of the low SNR of the Antarctica data; nonetheless the processing chain was still able to accurately discriminate the majority of lithological units with strong agreement to existing geological maps.

The results were validated and interpreted in the context of the study area in conjunction with a full suite of ancillary data: detailed high quality ground reference spectral data collected using a field portable Fourier transform infrared spectrometer, thin section and scanning electron microscope analysis, electron microprobe analysis, whole rock geochemical data and mineral modal analysis. The results are promising, with the thermal imagery allowing clear distinction between granitoid types. However, the distinction of fine grained, intermediate composition dykes is not possible due to the close spectral similarity with the country rock (granodiorite).

Acknowledgements

M Black is funded by a Natural Environment Research Council (NERC) PhD studentship in conjunction with the British Antarctic Survey (BAS) and the University of Hull (NERC Grant: NE/K50094X/1). The hyperspectral survey was funded by the UK Foreign and Commonwealth Office (FCO) and conducted by BAS, ITRES Research Ltd. and Defence Research & Development, Canada (DRDC). Fieldwork was supported by a Collaborative Gearing Scheme Grant (CGS-86). Field spectrometers were provided by the NERC Field Spectroscopy Facility (Loan No. 675.0613) and through Eldon Puckrin, DRDC. We gratefully acknowledge Eldon Puckrin, Stephen Achal and Alex Shipp for their support and assistance during fieldwork, and David Neave, Iris Buisman and Nick Marsh for their assistance with geochemical analysis.

References

Abrams, M., Hook, S. J., 1995. Simulated ASTER data for geologic studies. Geoscience and Remote Sensing, IEEE Transactions on 33 (3), 692–699.

Abrams, M. J., Ashley, R. P., Rowan, L. C., Goetz, A. F. H., Kahle, A. B., 1977. Mapping of hydrothermal alteration in the Cuprite mining district, Nevada, using aircraft scanner images for the spectral region 0.46 to 2.36 μm. Geology 5 (12), 713–718.

Adler, H. H., Kerr, P. F., 1963. Infrared absorption frequency trends for anhydrous normal carbonates. American Mineralogist 48 (1-2), 124.

Aslett, Z., Taranik, J. V., Riley, D. N., jul 2008. Mapping Rock-Forming Minerals at Daylight Pass, Death Valley National Park, California, using SEBASS Thermal-Infrared Hyperspectral Image Data. In: Geoscience and Remote Sensing Symposium, 2008. IGARSS 2008. IEEE International. Vol. 3. pp. III – 366–III – 369.

Benediktsson, J., Swain, P. H., Ersoy, O. K., 1990. Neural network approaches versus statistical methods in classification of multisource remote sensing data. IEEE Transactions on geoscience and remote sensing 28 (4), 540–552.

Berk, A., Anderson, G. P., Acharya, P. K., Bernstein, L. S., Muratov, L., Lee, J., Fox, M. J., Adler-Golden, S. M., Chetwynd, J. H., Hoke, M. L., Lockwood, R. B., Cooley,

T. W., Gardner, J. A., 2005. MODTRAN5: a reformulated atmospheric band model with auxiliary species and practical multiple scattering options.

Berman, M., Kiiveri, H., Lagerstrom, R., Ernst, A., Dunne, R., Huntington, J. F., 2004. ICE: A statistical approach to identifying endmembers in hyperspectral images: Learning from Earth's Shapes and Colors. IEEE transactions on Geoscience and Remote Sensing 42 (10), 2085–2095.

Bioucas-Dias, J. M., 2009. A variable splitting augmented Lagrangian approach to linear spectral unmixing. In: Hyperspectral Image and Signal Processing: Evolution in Remote Sensing, 2009. WHISPERS'09. First Workshop on. IEEE, Grenoble, France, pp. 1–4.

Black, M., Fleming, A., Riley, T., Ferrier, G., Fretwell, P., McFee, J., Achal, S., Diaz, A. U., 2014. On the Atmospheric Correction of Antarctic Airborne Hyperspectral Data. Remote Sensing 6 (5), 4498–4514.

Boardman, J. W., 1993. Automating spectral unmixing of AVIRIS data using convex geometry concepts. In: Summaries 4th Annu. JPL Airborne Geoscience Workshop. Vol. 1. JPL Publication 93–26, pp. 11–14.

Boardman, J. W., Kruse, F. A., 1994. Automated spectral analysis: A geologic example using AVIRIS data, North Grapevine Mountains, Nevada. Proceedings of tenth thematic conference on geologic remote sensing (pp. I407–I418), Environmental Research Institute of Michigan.

Calvin, W. M., Vaughan, R. G., Taranik, J. V., Smailbegovic, A., 2001. Mapping natural and human influenced acid sulfate weathering near Reno, NV using the SEBASS hyperspectral instrument. In: Geoscience and Remote Sensing Symposium, 2001. IGARSS '01. IEEE 2001 International. Vol. 2. pp. 727–729 vol.2.

Chan, T.-H., Chi, C.-Y., Huang, Y.-M., Ma, W.-K., nov 2009. A Convex Analysis-Based Minimum-Volume Enclosing Simplex Algorithm for Hyperspectral Unmixing. Signal Processing, IEEE Transactions on 57 (11), 4418–4432.

Chang, C. I., 2003. Hyperspectral Imaging: Techniques for Spectral Detection and Classification. Hyperspectral Imaging: Techniques for Spectral Detection and Classification. Springer US.

776 Chang, C.-I., Du, Q., 2004. Estimation of number of spectrally distinct signal sources
777 in hyperspectral imagery. Geoscience and Remote Sensing, IEEE Transactions on
778 42 (3), 608–619.

779 Chang, C.-I., Plaza, A., 2006. A fast iterative algorithm for implementation of pixel
780 purity index. Geoscience and Remote Sensing Letters, IEEE 3 (1), 63–67.

781 Chen, X., Warner, T. A., Campagna, D. J., oct 2007. Integrating visible, near-infrared
782 and short-wave infrared hyperspectral and multispectral thermal imagery for geolog-
783 ical mapping at Cuprite, Nevada. Remote Sensing of Environment 110 (3), 344–356.

784 Christensen, P. R., Bandfield, J. L., Hamilton, V. E., Howard, D. A., Lane, M. D.,
785 Piatek, J. L., Ruff, S. W., Stefanov, W. L., apr 2000. A thermal emission spectral
786 library of rock-forming minerals. Journal of Geophysical Research 105 (E4), 9735.

787 Clark, R. N., Swayze, G. A., 1996. Evolution in imaging spectroscopy analysis and
788 sensor signal-to-noise: An examination of how far we have come. In: Summaries
789 of the Sixth Annual JPL Airborne Earth Science Worksho, JPL Publication, March
790 4-8. pp. 4–8.

791 Clark, R. N., Swayze, G. A., Gallagher, A., 1993. Mapping minerals with imaging
792 spectroscopy. US Geological Survey, Office of Mineral Resources Bulletin 2039,
793 141–150.

794 Craig, M. D., 1994. Minimum-volume transforms for remotely sensed data. Geo-
795 science and Remote Sensing, IEEE Transactions on 32 (3), 542–552.

796 Cudahy, T. J., Wilson, J., Hewson, R., Linton, P., Harris, P., Sears, M., Okada, K.,
797 Hackwell, J. A., 2001. Mapping porphyry-skarn alteration at Yerington, Nevada,
798 using airborne hyperspectral VNIR-SWIR-TIR imaging data. In: Geoscience and
799 Remote Sensing Symposium, 2001. IGARSS '01. IEEE 2001 International. Vol. 2.
800 pp. 631–633.

801 Dash, P., Göttsche, F.-M., Olesen, F.-S., Fischer, H., jan 2002. Land surface tempera-
802 ture and emissivity estimation from passive sensor data: Theory and practice-current
803 trends. International Journal of Remote Sensing 23 (13), 2563–2594.

804 Distasio Jr., R., Resmini, R., apr 2010. Atmospheric compensation of thermal infrared
805 hyperspectral imagery with the emissive empirical line method and the in-scene at-

mospheric compensation algorithms: a comparison. In: Society of Photo-Optical Instrumentation Engineers (SPIE) Conference Series. Vol. 7695 of Society of Photo-Optical Instrumentation Engineers (SPIE) Conference Series.

Drury, S. A., 2001. Image Interpretation in Geology. Blackwell Science, Oxford, UK.

Feely, K. C., Christensen, P. R., 1999. Quantitative compositional analysis using thermal emission spectroscopy: Application to igneous and metamorphic rocks. Journal of Geophysical Research: Planets (1991–2012) 104 (E10), 24195–24210.

Felzenszwalb, P. F., Huttenlocher, D. P., 2004. Efficient graph-based image segmentation. International Journal of Computer Vision 59 (2), 167–181.

Feng, J., Rivard, B., Rogge, D. M., Grant, B., jun 2012. Spectral enhancement of sebass hyperspectral data and its application in mapping of ultramafic rocks. In: 4th Workshop on Hyperspectral Image and Signal Processing: Evolution in Remote Sensing (WHISPERS). pp. 1–4.

Freemantle, J. R., Pu, R., Miller, J. R., 1992. Calibration of imaging spectrometer data to reflectance using pseudo-invariant features. In: Proceedings of the 14th Canadian Symposium on Remote Sensing. pp. 1–4.

Galehouse, J., 1971. Point counting. In: Carver, R. E. (Ed.), Procedures in Sedimentary Petrology. John Wiley and Sons Canada, Limited.

Gillespie, a., Rokugawa, S., Matsunaga, T., Cothern, J., Hook, S., Kahle, A., jul 1998. A temperature and emissivity separation algorithm for Advanced Spaceborne Thermal Emission and Reflection Radiometer (ASTER) images. IEEE Transactions on Geoscience and Remote Sensing 36 (4), 1113–1126.

Gilmore, M. S., Thompson, D. R., Anderson, L. J., Karamzadeh, N., Mandrake, L., Castaño, R., 2011. Superpixel segmentation for analysis of hyperspectral data sets, with application to Compact Reconnaissance Imaging Spectrometer for Mars data, Moon Mineralogy Mapper data, and Ariadnes Chaos, Mars. Journal of Geophysical Research: Planets 116 (E7).

Green, R. O., Eastwood, M. L., Sarture, C. M., Chrien, T. G., Aronsson, M., Chippendale, B. J., Faust, J. A., Pavri, B. E., Chovit, C. J., Solis, M., Others, 1998. Imaging

spectroscopy and the airborne visible/infrared imaging spectrometer (AVIRIS). Remote Sensing of Environment 65 (3), 227–248.

Guilfoyle, K. J., Althouse, M. L., Chang, C.-I., 2001. A quantitative and comparative analysis of linear and nonlinear spectral mixture models using radial basis function neural networks. Geoscience and Remote Sensing, IEEE Transactions on 39 (10), 2314–2318.

Gupta, R. P., 2003. Remote Sensing Geology. Springer-Verlag, Berlin, Germany.

Hamilton, V. E., Christensen, P. R., 2000. Determining the modal mineralogy of mafic and ultramafic igneous rocks using thermal emission spectroscopy. Journal of Geophysical Research 105 (E4), 9717–9733.

Harris, J. R., Rogge, D., Hitchcock, R., Ijewlie, O., Wright, D., 2005. Mapping lithology in Canada's Arctic: application of hyperspectral data using the minimum noise fraction transformation and matched filtering. Canadian Journal of Remote Sensing 2193 (2005), 2173–2193.

Haselwimmer, C. E., Riley, T. R., Liu, J. G., feb 2010. Assessing the potential of multispectral remote sensing for lithological mapping on the Antarctic Peninsula: case study from eastern Adelaide Island, Graham Land. Antarctic Science 22 (03), 299–318.

Haselwimmer, C. E., Riley, T. R., Liu, J. G., mar 2011. Lithologic mapping in the Oscar II Coast area, Graham Land, Antarctic Peninsula using ASTER data. International Journal of Remote Sensing 32 (7), 2013–2035.

Hecker, C., Dilles, J. H., van der Meijde, M., van der Meer, F. D., 2012. Thermal infrared spectroscopy and partial least squares regression to determine mineral modes of granitoid rocks. Geochemistry, Geophysics, Geosystems 13 (3), Q03021.

Hecker, C., van der Meijde, M., van der Meer, F. D., nov 2010. Thermal infrared spectroscopy on feldspars - Successes, limitations and their implications for remote sensing. Earth-Science Reviews 103 (1-2), 60–70.

Heinz, D. C., Chang, C.-I., 2001. Fully constrained least squares linear spectral mixture analysis method for material quantification in hyperspectral imagery. Geoscience and Remote Sensing, IEEE Transactions on 39 (3), 529–545.

Hewson, R., Hausknecht, P., Cudahy, T., Huntington, J., Mason, P., Hackwell, J., Nikitas, J., Okada, K., 2000. An Appraisal of the Hyperspectral Thermal-infrared SEBASS Data Recorded from Oatman, Arizona and a Comparison of Their Unmixed Results with AVIRIS. Exploration and mining report 668F. CSIRO Exploration and Mining, Wembley, Western Australia.

Hook, S. J., Cudahy, T. J., Kahle, A. B., Whitbourn, L. B., 1998. Synergy of active and passive airborne thermal infrared systems for surface compositional mapping. Journal of Geophysical Research: Solid Earth (1978–2012) 103 (B8), 18269–18276.

Hook, S. J., Dmochowski, J. E., Howard, K. A., Rowan, L. C., Karlstrom, K. E., Stock, J. M., apr 2005. Mapping variations in weight percent silica measured from multispectral thermal infrared imagery - Examples from the Hiller Mountains, Nevada, USA and Tres Virgenes-La Reforma, Baja California Sur, Mexico. Remote Sensing of Environment 95 (3), 273–289.

Hook, S. J., Elvidge, C. D., Rast, M., Watanabe, H., 1991. An evaluation of shortwave-infrared (SWIR) data from the AVIRIS and GEOSCAN instruments for mineralogical mapping at Cuprite, Nevada. Geophysics 56 (9), 1432–1440.

Hook, S. J., Rast, M., 1990. Mineralogic mapping using Airborne Visible Infrared Imaging Spectrometer (AVIRIS), Shortwave Infrared (SWIR) data acquired over Cuprite, Nevada. In: Proceedings of the Second Airborne Visible Infrared Imaging Spectrometer (AVIRIS) Workshop, JPL Publication. pp. 54–90.

Hulley, G., Realmuto, V., Hook, S., Ramsey, M., oct 2012. HyspIRI Thermal Infrared (TIR) Band Study Report. Tech. rep., NASA Jet Propulsion Laboratory, California.

Hunt, G., Salisbury, J., jul 1975. Mid-infrared spectral behavior of sedimentary rocks. Tech. rep.

Hunt, G. R., 1980. Electromagnetic radiation: the communication link in remote sensing. Remote sensing in geology 2, 5–45.

Keshava, N., Mustard, J. F., 2002. Spectral unmixing. Signal Processing Magazine, IEEE 19 (1), 44–57.

Kramer, H. J., 2002. Observation of the Earth and Its Environment: Survey of Missions and Sensors. Engineering online library. Springer.

Kruse, F., Lefkoff, A., Boardman, J., Heidebrecht, K., Shapiro, A., Barloon, P., Goetz, A., may 1993a. The spectral image processing system (SIPS)interactive visualization and analysis of imaging spectrometer data. Remote Sensing of Environment 44 (2-3), 145–163.

Kruse, F. A., Kierein-Young, K. S., Boardman, J. W., 1990. Mineral mapping at Cuprite, Nevada with a 63-channel imaging spectrometer. Photogrammetric Engineering and Remote Sensing 56, 83–92.

Kruse, F. A., Lefkoff, A. B., Dietz, J. B., 1993b. Expert system-based mineral mapping in northern Death Valley, California/Nevada, using the airborne visible/infrared imaging spectrometer (AVIRIS). Remote Sensing of Environment 44 (2), 309–336.

Kruse, F. A., McDowell, M., may 2015. Analysis of multispectral and hyperspectral longwave infrared (LWIR) data for geologic mapping. In: Velez-Reyes, M., Kruse, F. A. (Eds.), Proc. SPIE 9472, Algorithms and Technologies for Multispectral, Hyperspectral, and Ultraspectral Imagery XXI. p. 94721E.

Lane, M. D., Christensen, P. R., nov 1997. Thermal infrared emission spectroscopy of anhydrous carbonates. Journal of Geophysical Research 102 (E11), 25581.

Li, J., Bioucas-Dias, J. M., jul 2008. Minimum Volume Simplex Analysis: A Fast Algorithm to Unmix Hyperspectral Data. In: Geoscience and Remote Sensing Symposium, IEEE International. Boston, Massachusetts, USA. Vol. 3. pp. 250–253.

Liang, S., Fang, H., Chen, M., Shuey, C. J., Walthall, C., Daughtry, C., Morisette, J., Schaaf, C., Strahler, A., 2002. Validating MODIS land surface reflectance and albedo products: methods and preliminary results. Remote Sensing of Environment 83 (1-2), 149–162.

MathWorks, 2011. MATLAB, version 7.12.0.635 (R2011a). The MathWorks Inc., Natick, Massachusetts.

Miao, L., Qi, H., 2007. Endmember extraction from highly mixed data using minimum volume constrained nonnegative matrix factorization. Geoscience and Remote Sensing, IEEE Transactions on 45 (3), 765–777.

Milam, K. A., McSween, H. Y., Hamilton, V. E., Moersch, J. M., Christensen, P. R., 2004. Accuracy of plagioclase compositions from laboratory and Mars spacecraft

thermal emission spectra. Journal of Geophysical Research: Planets (1991–2012) 109 (E4).

Nascimento, J. M. P., Bioucas-Dias, J. M., 2005. Vertex component analysis: A fast algorithm to unmix hyperspectral data. Geoscience and Remote Sensing, IEEE Transactions on 43 (4), 898–910.

Philpot, W., Ansty, T., jul 2011. Analytical description of pseudo-invariant features (PIFs). In: 6th International Workshop on Analysis of Multi-temporal Remote Sensing Images (Multi-Temp). pp. 53–56.

Plaza, A., Benediktsson, J. A., Boardman, J. W., Brazile, J., Bruzzone, L., Camps-Valls, G., Chanussot, J., Fauvel, M., Gamba, P., Gualtieri, A., Marconcini, M., Tilton, J. C., Trianni, G., sep 2009. Recent advances in techniques for hyperspectral image processing. Remote Sensing of Environment 113, S110–S122.

Plaza, A., Plaza, J., Martínez, G., Sanchez, S., 2011. Hyperspectral Data Processing Algorithms. In: Thenkabail, P. S., Lyon, J. G., Huete, A. (Eds.), Hyperspectral Remote Sensing of Vegetation. CRC Press, Ch. 5, pp. 121–138.

Plaza, J., Hendrix, E. M. T., García, I., Martín, G., Plaza, A., 2012. On endmember identification in hyperspectral images without pure pixels: A comparison of algorithms. Journal of Mathematical Imaging and Vision 42 (2-3), 163–175.

Plaza, J., Plaza, A., Perez, R., Martinez, P., 2008. Parallel Classification of Hyperspectral Images Using Neural Networks. In: Grana, M., Duro, R. J. (Eds.), Computational Intelligence for Remote Sensing. Springer, Ch. 8, pp. 193–216.

Resmini, R. G., Kappus, M. E., Aldrich, W. S., Harsanyi, J. C., Anderson, M., 1997. Mineral mapping with hyperspectral digital imagery collection experiment (HYDICE) sensor data at Cuprite, Nevada, USA. International Journal of Remote Sensing 18 (7), 1553–1570.

Richter, R., Coll, C., jun 2002. Bandpass-Resampling Effects for the Retrieval of Surface Emissivity. Applied Optics 41 (18), 3523–3529.

Richter, R., Schläpfer, D., 2002. Geo-atmospheric processing of airborne imaging spectrometry data. Part 2: Atmospheric/topographic correction. International Journal of Remote Sensing 23 (13), 2631–2649.

955 Richter, R., Schläpfer, D., 2014. Atmospheric / Topographic Correction for Airborne
956 Imagery. ATCOR-4 User Guide, Version 6.2.1. DLR-IB 565-02/08. Deutsches Zen-
957 trum für Luft- und Raumfahrt (DLR), Weßling, Germany.

958 Riley, D. N., Hecker, C. A., 2013. Mineral mapping with airborne hyperspectral ther-
959 mal infrared remote sensing at Cuprite, Nevada, USA. In: Thermal Infrared Remote
960 Sensing. Springer, pp. 495–514.

961 Rivard, B., Zhang, J., Feng, J., Sanchez-Azofeifa, G. A., 2009. Remote predictive litho-
962 logic mapping in the Abitibi Greenstone Belt, Canada, using airborne hyperspectral
963 imagery. Canadian Journal of Remote Sensing 35 (sup1), S95–S105.

964 Rogge, D., Rivard, B., dec 2006. Iterative spectral unmixing for optimizing per-pixel
965 endmember sets. Geoscience and Remote Sensing, IEEE 44 (12), 3725–3736.

966 Rogge, D., Rivard, B., Harris, J., Zhang, J., 2009. Application of hyperspectral data for
967 remote predictive mapping, Baffin Island, Canada. Reviews in Economic Geology
968 16, 209–222.

969 Rowan, L. C., Hook, S. J., Abrams, M. J., Mars, J. C., 2003. Mapping hydrothermally
970 altered rocks at Cuprite, Nevada, using the Advanced Spaceborne Thermal Emission
971 and Reflection Radiometer (ASTER), a new satellite-imaging system. Economic Ge-
972 ology 98 (5), 1019–1027.

973 Rowan, L. C., Mars, J. C., mar 2003. Lithologic mapping in the Mountain Pass, Califor-
974 nia area using Advanced Spaceborne Thermal Emission and Reflection Radiometer
975 (ASTER) data. Remote Sensing of Environment 84 (3), 350–366.

976 Salisbury, J. W., 1991. Infrared (2.1-25 um) spectra of minerals. Johns Hopkins studies
977 in earth and space sciences. Johns Hopkins University Press.

978 Salvaggio, C., Miller, C. J., 2001. Methodologies and protocols for the collection of
979 midwave and longwave infrared emissivity spectra using a portable field spectrome-
980 ter.

981 Salvatore, M. R., Mustard, J. F., Head, J. W. I. I. I., Marchant, D. R., Wyatt, M. B.,
982 2014. Characterization of spectral and geochemical variability within the Ferrar Do-
983 lerite of the McMurdo Dry Valleys, Antarctica: weathering, alteration, and magmatic
984 processes. Antarctic Science 26 (01), 49–68.

985 Shimoni, M., van der Meer, F., Acheroy, M., 2007. Thermal imaging spectroscopy:
986 Present technology and future dual use applications. In: Proceedings 5th EARSeL
987 Workshop on Imaging Spectroscopy. Bruges, Belgium.

988 Smith, G. M., Milton, E. J., 1999. The use of the empirical line method to calibrate
989 remotely sensed data to reflectance. International Journal of Remote Sensing 20 (13),
990 2659–2662.

991 Thompson, D. R., Bornstein, B. J., Chien, S. A., Schaffer, S., Tran, D., Bue, B. D.,
992 Castano, R., Gleeson, D. F., Noell, A., jun 2013. Autonomous Spectral Discovery
993 and Mapping Onboard the EO-1 Spacecraft. Geoscience and Remote Sensing, IEEE
994 Transactions on 51 (6), 3567–3579.

995 Thompson, D. R., Mandrake, L., Gilmore, M. S., Castano, R., nov 2010. Super-
996 pixel Endmember Detection. Geoscience and Remote Sensing, IEEE Transactions
997 on 48 (11), 4023–4033.

998 Tuominen, J., Lipping, T., 2011. Atmospheric correction of hyperspectral data using
999 combined empirical and model based method. In: EARSeL 7th SIG-Imaging Spec-
1000 troscopy Workshop.

1001 van der Meer, F. D., 1995. Spectral reflectance of carbonate mineral mixtures and bidi-
1002 rectional reflectance theory: Quantitative analysis techniques for application in re-
1003 mote sensing. Remote Sensing Reviews 13 (1-2), 67–94.

1004 van der Meer, F. D., van der Werff, H. M., van Ruitenbeek, F. J., Hecker, C. a., Bakker,
1005 W. H., Noomen, M. F., van der Meijde, M., Carranza, E. J. M., Smeth, J. B. D.,
1006 Woldai, T., feb 2012. Multi- and hyperspectral geologic remote sensing: A review.
1007 International Journal of Applied Earth Observation and Geoinformation 14 (1), 112–
1008 128.

1009 Vaughan, R., Calvin, W. M., Taranik, J. V., apr 2003. SEBASS hyperspectral thermal
1010 infrared data: surface emissivity measurement and mineral mapping. Remote Sens-
1011 ing of Environment 85 (1), 48–63.

1012 Vaughan, R. G., Hook, S. J., Calvin, W. M., Taranik, J. V., nov 2005. Surface min-
1013 eral mapping at Steamboat Springs, Nevada, USA, with multi-wavelength thermal
1014 infrared images. Remote Sensing of Environment 99 (1-2), 140–158.

Winter, M. E., 1999. N-FINDR: an algorithm for fast autonomous spectral end-member determination in hyperspectral data. In: SPIE's International Symposium on Optical Science, Engineering, and Instrumentation. International Society for Optics and Photonics, pp. 266–275.

Table 1: Geochemical analyses of Anchorage Island samples from XRF spectroscopy.
† total iron (FeO and Fe_2O_3).

Sample	J13.22.10	J13.19.10	J13.22.5	J13.21.10
Unit	Dolerite	Granodiorite		Granite
Major elements (%)				
SiO_2	54.40	55.19	59.59	78.29
TiO_2	1.02	0.94	0.87	0.20
Al_2O_3	16.62	18.18	16.35	11.64
Fe_2O_3†	8.66	8.55	6.67	0.86
MnO	0.124	0.112	0.147	0.013
MgO	3.96	3.29	3.52	0.16
CaO	8.57	7.49	6.16	0.53
Na_2O	3.14	4.04	3.51	2.74
K_2O	0.958	1.066	2.115	5.610
P_2O_5	0.241	0.176	0.185	0.018
SO_3	0.170	0.009	< 0.003	< 0.003
LOI	2.05	0.88	0.97	0.31
Total	99.92	99.93	100.09	100.38
Trace elements (ppm)				
As	6.7	8.4	5.1	4.4
Ba	365.0	432.2	698.4	475.5
Ce	44.2	27.9	48.4	11.4
Co	25.7	18.3	21.6	< 1.1
Cr	112.0	6.4	37.0	< 0.6
Cu	110.8	19.9	32.8	3.5
Ga	18.2	21.2	17.8	9.9
La	20.0	13.7	21.3	7.9
Mo	3.9	2.3	3.3	0.9
Nb	4.8	4.4	6.8	4.7
Nd	23.6	16.7	25.2	7.7
Ni	12.8	< 0.7	18.7	< 0.5
Pb	8.2	9.7	7.5	9.7
Rb	15.6	36.7	55.6	140.3
Sc	30.6	34.1	23.1	3.3
Sr	458.2	481.4	415.7	111.2
Th	6.9	3.5	10.2	17.3
U	2.6	1.3	1.4	2.5
V	229.0	267.8	159.2	10.9
Y	30.8	27.1	29.6	20.7
Zn	48.8	71.2	72.4	14.8
Zr	179.1	43.3	230.9	98.2

Table 2: Results from point counting, where mineral counts are given as percentages. A total of 500 points were counted on each sample (n=500).

Sample	J13.22.5	J13.22.10	J13.21.10
Unit	Granodiorite	Dolerite	Granite
Point Count (%)			
Biotite			1.2
Chlorite	8.8		
Clinopyroxene		33	
Hornblende	12.6		
K-Feldspar			27.8
Muscovite		1.4	
Opaques	1	4.6	1
Plagioclase	44.8	61	35
Quartz	32.8		35

Table 3: Root Mean Square Error statistics.

RMSE (%)	Mean	Max	StDev
Endmember-1	0.498	7.830	0.464
Endmember-2	0.473	3.447	0.439
Endmember-3	0.939	23.223	1.246
Endmember-5	0.425	5.952	0.451
All Endmembers	0.584	23.223	0.650

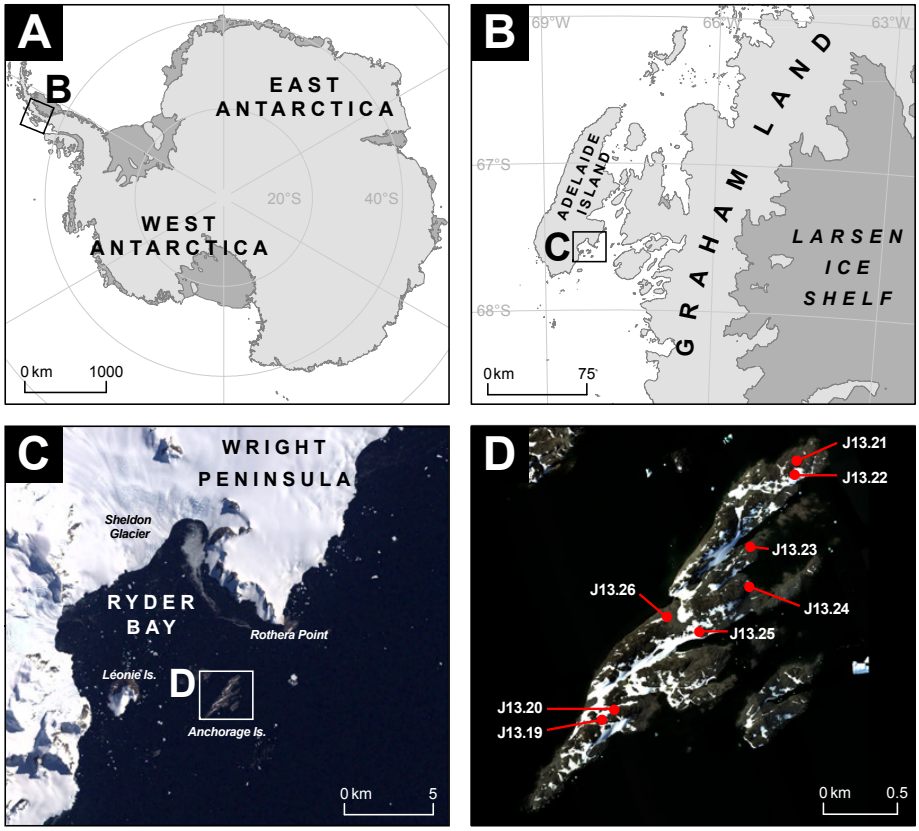

Figure 1: Location maps showing the context of the study area within Antarctica (A), the location of Adelaide Island within the Antarctic Peninsula (B) and the location of Anchorage Island in the context of Ryder Bay (C; labelled). (D) shows a true colour composite of Anchorage Island with field localities (labelled red circles).

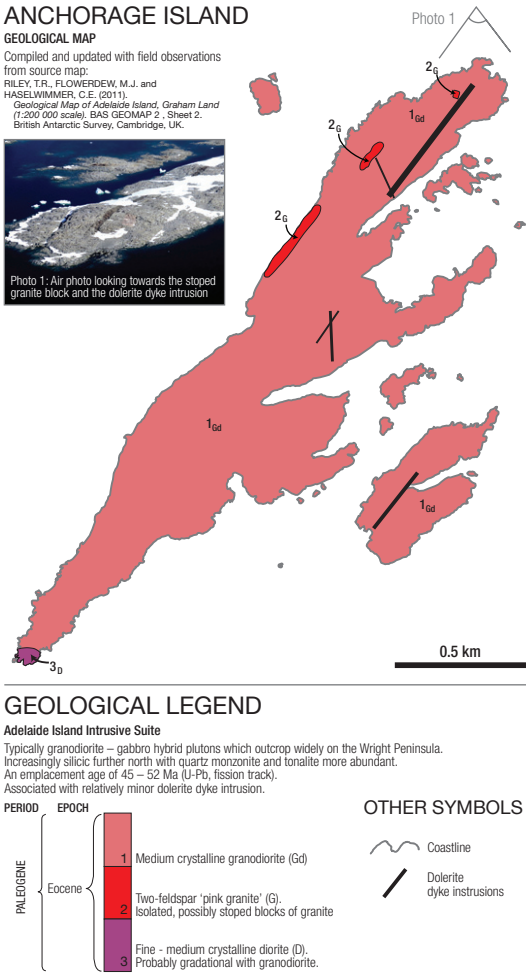

Figure 2: Local scale geological map of Anchorage Island.

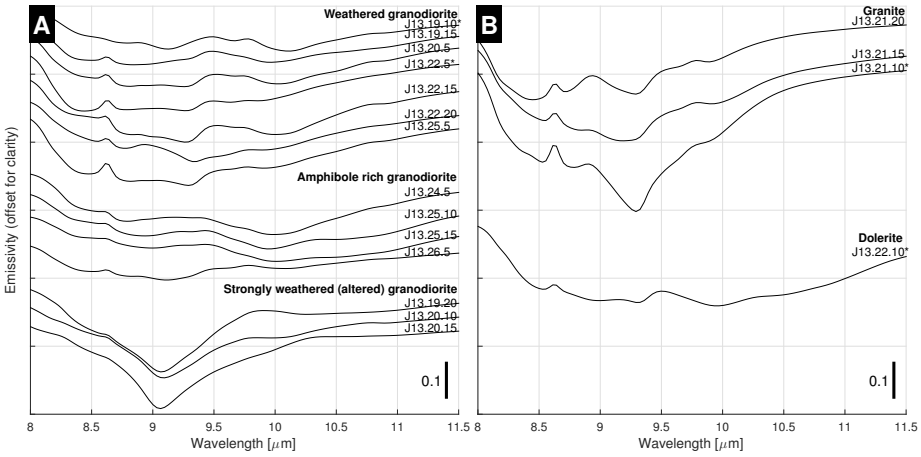

Figure 3: Spectral emissivity measured in the field using a Fourier Transform Infrared Spectrometer (FTIR) of relevant lithological units from Anchorage Island. (A) shows granodiorite spectra (B) shows granite and dolerite spectra.

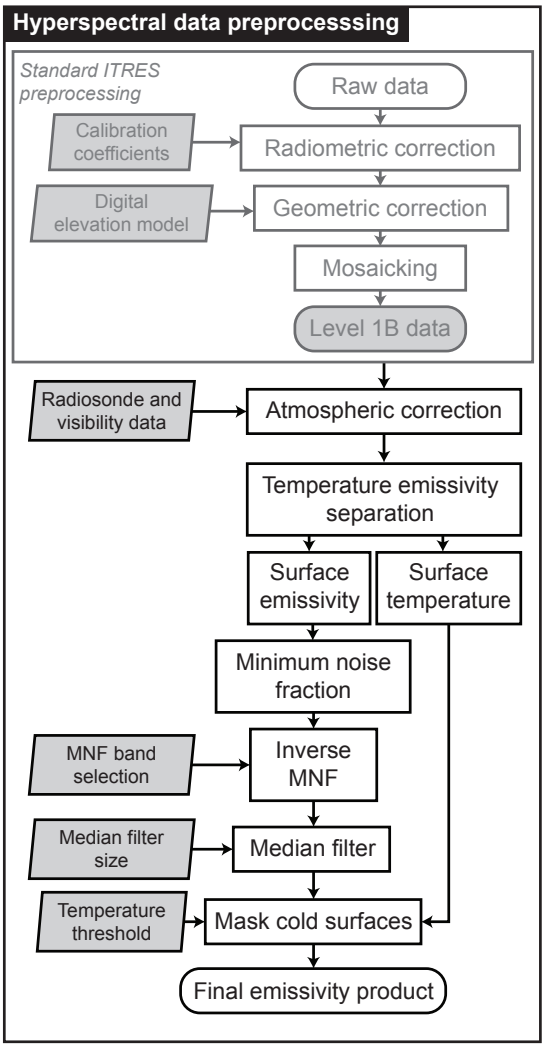

Figure 4: Flow chart summarising the preprocessing of the hyperspectral imagery. Inputs and parameters are shown in the left column (light grey boxes). Abbreviated processing steps are as follows: MNF, minimum noise fraction.

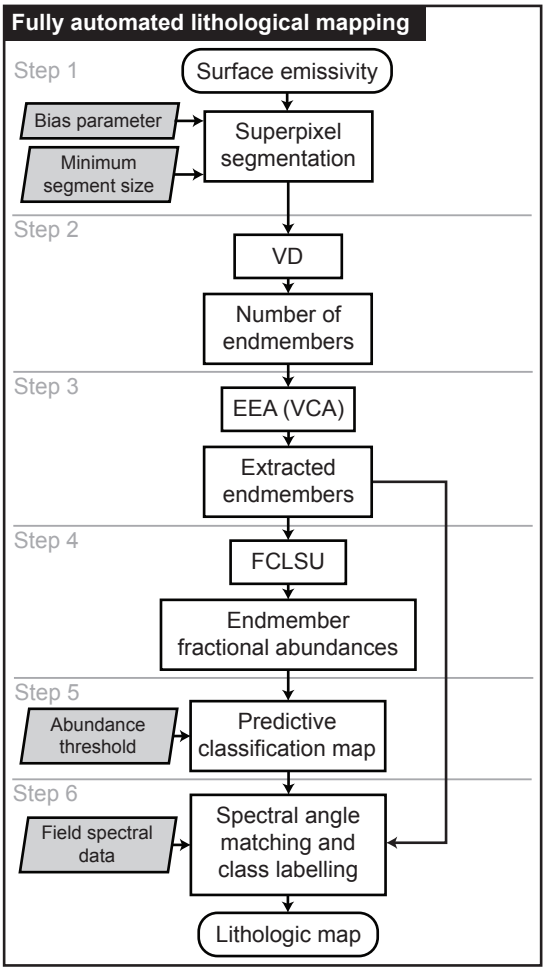

Figure 5: Flow chart summarising the methods of the fully automated lithological mapping process. Inputs and parameters are shown in the left column (light grey boxes). Abbreviated processing steps are as follows: VD, virtual dimensionality; EEA, endmember extraction algorithm; VCA, vertex component analysis; FCLSU, fully constrained linear spectral unmixing.

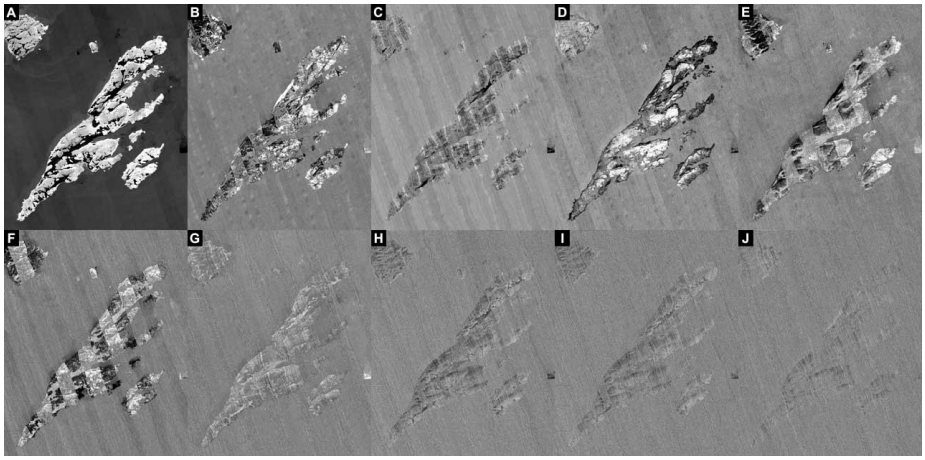

Figure 6: Images for the first 10 components of the Minimum Noise Fraction (MNF) transform (A-J). Components 1 to 4 (A to D) were utilised in the inverse MNF procedure.

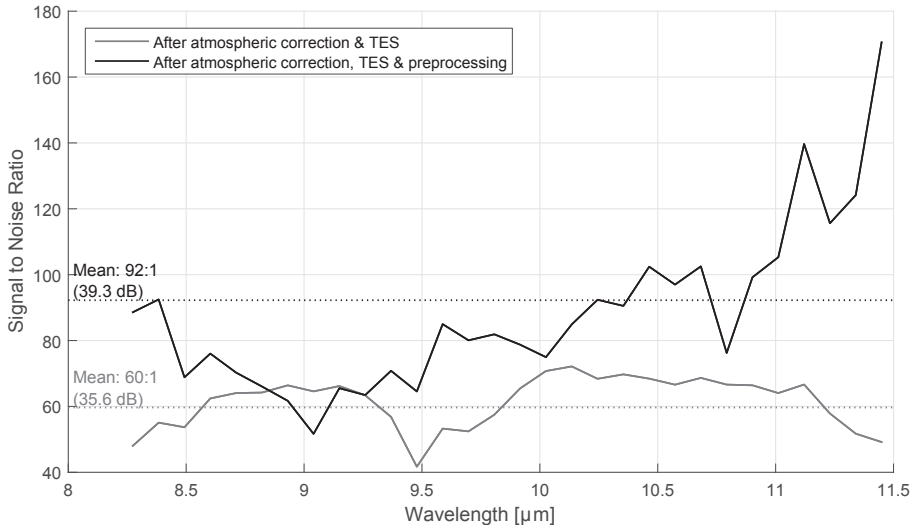

Figure 7: Signal to noise ratio (SNR) calculated from the image after atmospheric correction and temperature emissivity separation (TES; grey line) compared to the SNR for the final image after all preprocessing (atmospheric correction, TES, emissive empirical line correction and minimum noise fraction for noise reduction) (black line). Mean values are shown in the annotations.

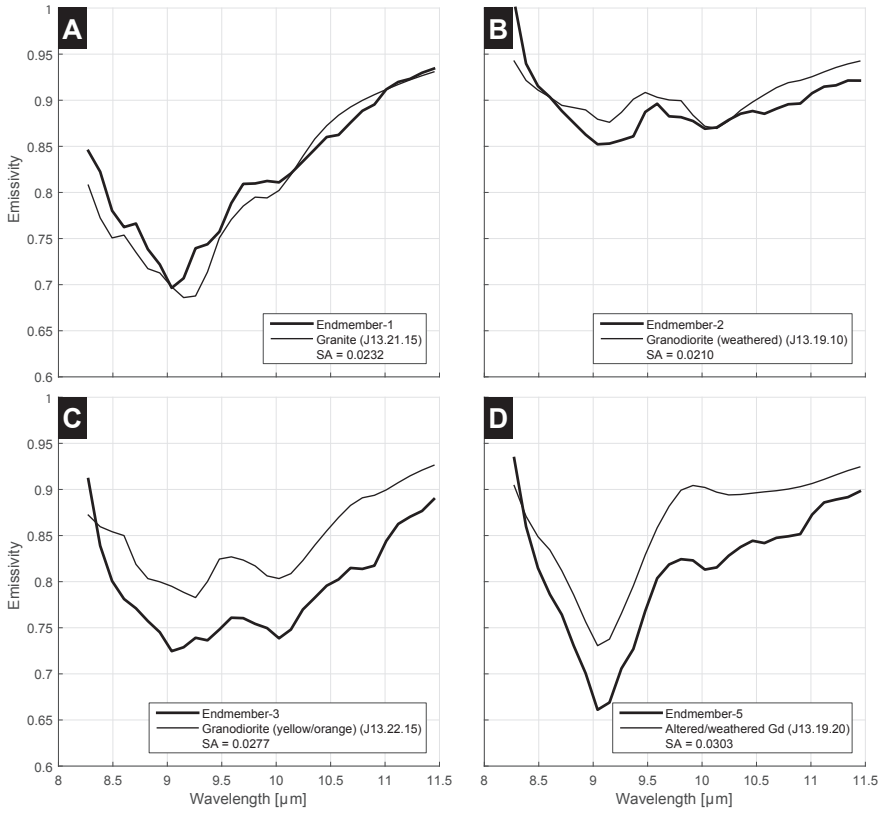

Figure 8: Four extracted endmembers (thick line) and their closest match from the field spectral data (thin line). The spectral angle (SA), in radians, is shown in each figure legend.

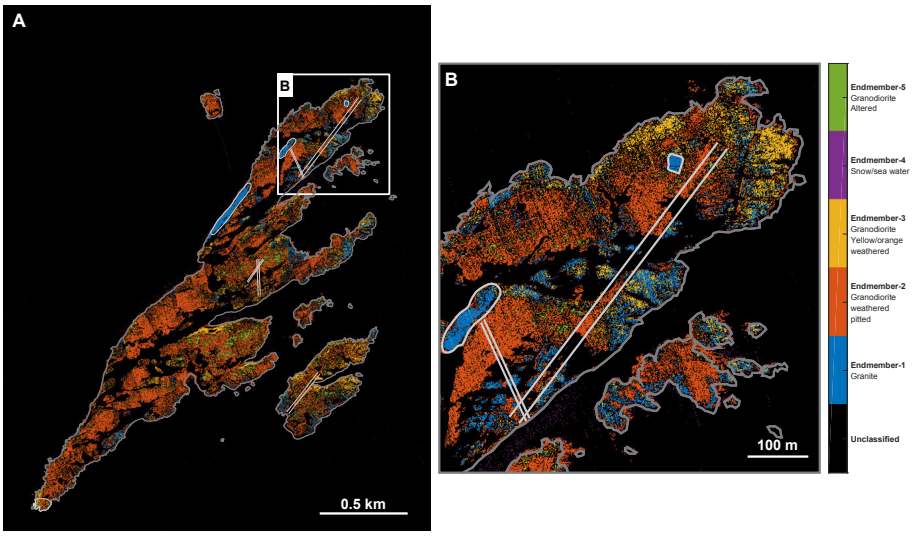

Figure 9: Lithological map generated from the automated processing chain. (A) shows the whole of Anchorage Island and inset (B) shows an area of interest around a stoped granite block in the North East of Anchorage Isalnd. Compare Figure 2 for geological boundaries.

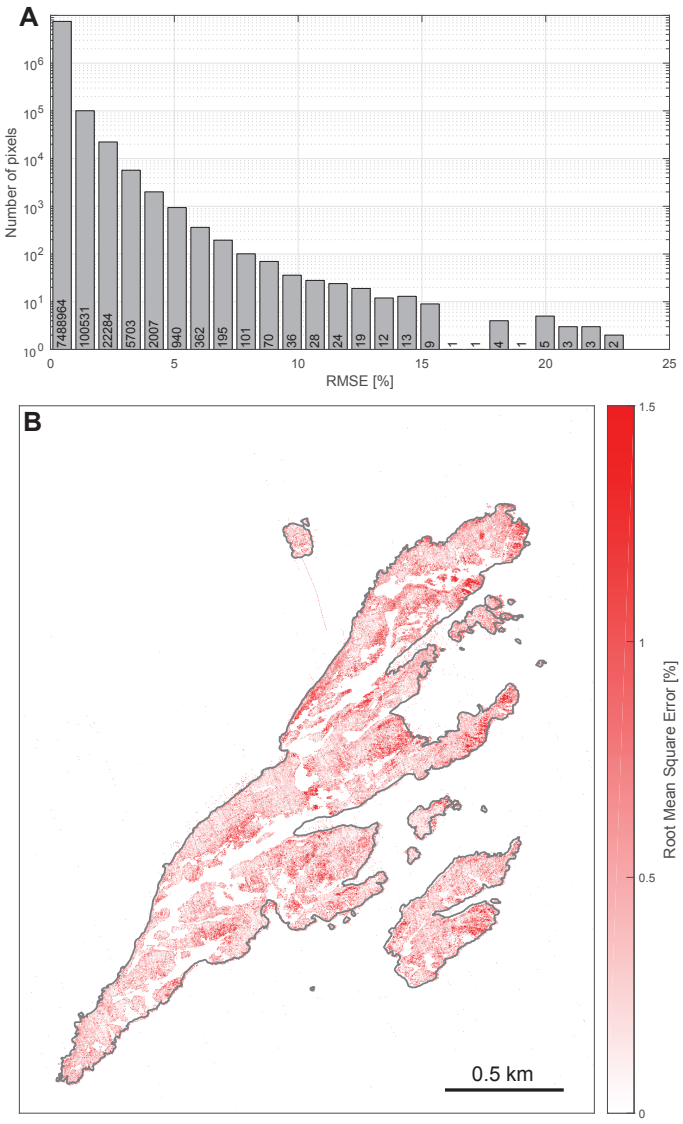

Figure 10: (A) histogram of Root Mean Square Error (RMSE; %) values; note the log scale. (B) shows the RMSE image of Anchorage Island. Note: the colorbar is capped at 1.5% as the predominant distribution of RMSE values is below this threshold.

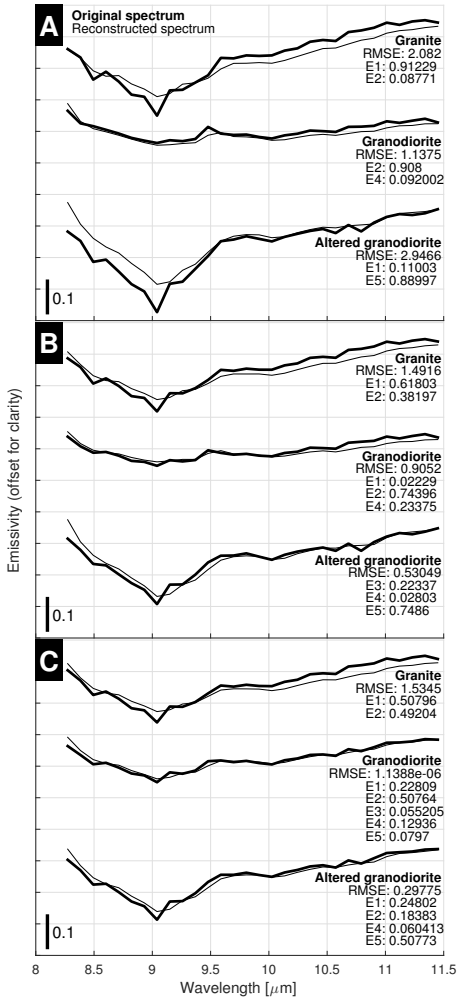

Figure 11: Original image spectra (bold line) and their reconstructed spectra (thin line; calculated using the endmember spectra and the fractional abundances). Figure annotations are as follows: RMSE; root mean square error, %; E1 to E5; fractional abundances of endmember-1 to endmember-5. (A) high purity (0.9 fractional abundance) spectra, (B) medium purity (0.75 fractional abundance) spectra and (C) low purity (0.5 fractional abundance) spectra.